13

Example of a general-purpose detector: Belle

Our job in physics is to see things simply, to understand a great many complicated phenomena, in terms of a few simple principles.

Steven Weinberg

A present-day experiment in high energy physics usually requires a multipurpose experimental setup consisting of at least several (or many) subsystems. This setup (called commonly 'detector') contains a multitude of sensitive channels which are necessary to measure the characteristics of particles produced in collisions or decays of the initial particles. A typical set of detector properties includes abilities of tracking, i.e. measurement of vertex coordinates and charged-particle angles, measurements of charged-particle momenta, particle energy determination and particle identification. A very important system is the trigger which detects the occurrence of an event of interest and produces a signal to start the readout of the information from the relevant channels. Since high energy physics experiments are running for months or years, the important task is to monitor and control the parameters of the detector and to keep them as stable as possible. To fulfil this task the detector is usually equipped with a so-called *slow control system*, which continuously records hundreds of experimental parameters and warns experimentalists if some of them are beyond certain boundaries.

To control the process of accumulating statistics and calculating the cross sections and decay rates, a luminosity measurement system is mandatory (for the term definition, see Chap. 4).

One of the general-purpose detectors, Belle, is discussed in this chapter. The Belle detector for experiments at the KEKB, an energy-asymmetric B factory with high luminosity, has been constructed at KEK in Tsukuba, Japan, to study CP violation in B-meson decays. The KEKB e^+e^- collider [1] is based on two separate rings for electrons (8 GeV) and positrons (3.5 GeV) installed in a tunnel with a circumference of about 3 km.

https://doi.org/10.1017/9781009401531.016 Published online by Cambridge University Press

The present luminosity is about $1.6 \cdot 10^{34}\,\mathrm{cm}^{-2}\,\mathrm{s}^{-1}$ which is achieved at a 2 A positron current and a 1.5 A electron current.

The Belle detector was constructed in 1994–8. Since 1999, the detector has been running and by now (beginning of 2007) this experiment has collected about $700\,\mathrm{fb}^{-1}$ of integrated luminosity.

13.1 Detector components

The detector layout is shown in Fig. 13.1 and its detailed description can be found in [2]. Most results reported in this chapter are taken from [2].

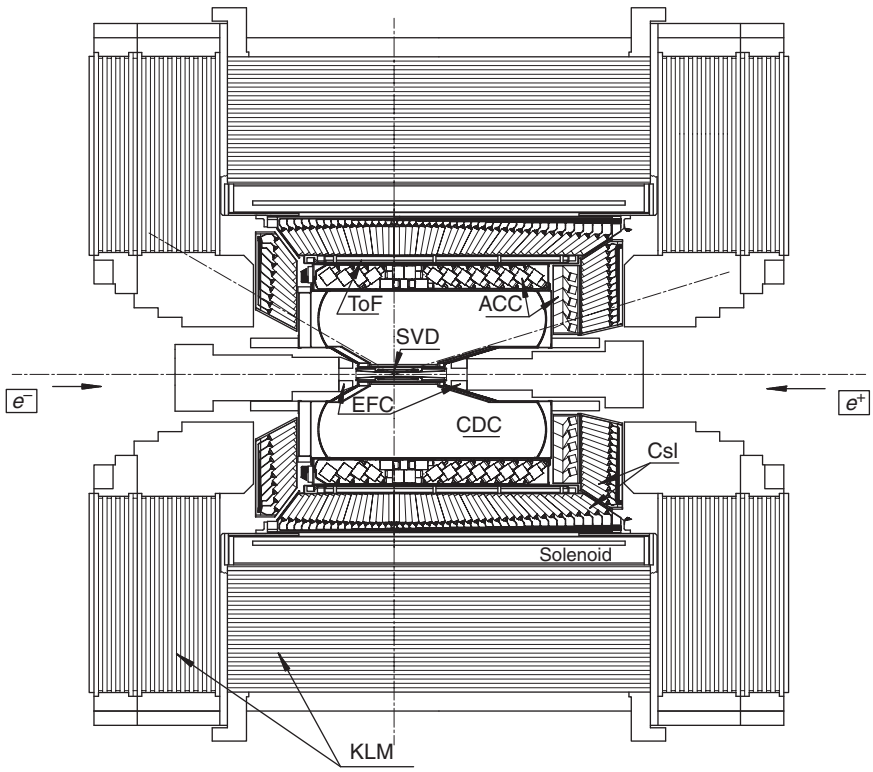

Beam Pipe	double wall of 0.5 mm beryllium, *He*-gas cooled
SVD	3 layers of double-sided 300 μ-silicon sensors
CDC	50 anode layers (18 stereo), 3 cathode layers
ACC	960 + 228 aerogel cells, $n = 1.01$–1.03
ToF	4 cm-thick scintillator, 128 ϕ segmentation
CsI	6624 + 1152 + 960 CsI(Tl) crystals, 30 cm long
Solenoid	1.5 T
KLM	14 layers of RPC superlayer and 4.7 cm iron
EFC	160 (13.7 cm) + 160 (12.4 cm) BGO crystals

Fig. 13.1. Schematic view of the Belle detector [2].

https://doi.org/10.1017/9781009401531.016 Published online by Cambridge University Press

The electron and positron beams cross at an angle of ±11 mrad inside the beam pipe. The central part ($-4.6\,\mathrm{cm} \leq z \leq 10.1\,\mathrm{cm}$) of the beam pipe is a double-wall beryllium cylinder with an inner diameter of 30 mm. A 2.5 mm gap between the inner and outer walls of the cylinder provides a helium gas channel for cooling. Each wall has a thickness of 0.5 mm.

B-meson decay vertices are measured by a silicon vertex detector (SVD) situated just outside the beam pipe. Charged-particle tracking is provided by a 50-layer wire drift chamber (central drift chamber, CDC). Particle identification is based on $\mathrm{d}E/\mathrm{d}x$ measurements in the CDC, in aerogel Cherenkov counters (ACC) and time-of-flight counters (TOF) placed radially outside of the central drift chamber. Electromagnetic showers are detected in an array of thallium-doped caesium-iodide counters (CsI(Tl); electromagnetic calorimeter, ECL). All mentioned subdetectors are located inside a 3.4 m-diameter superconducting solenoid which provides an axial 1.5 T magnetic field.

Muons and K_L mesons are identified by arrays of resistive-plate counters interleaved in the iron yoke (K_L and muon detection system, KLM). The detector covers a θ region extending from 17° to 150°, where θ is the angle with respect to the beam axis. Part of the otherwise uncovered small-angle region is instrumented with a pair of bismuth-germanate (BGO) crystal arrays (electron forward calorimeter, EFC) placed on the surfaces of the cryostats of the focussing quadrupole lenses in the forward and backward directions.

13.1.1 The silicon vertex detector (SVD)

Since most particles of interest in Belle have momenta of $1\,\mathrm{GeV}/c$ or less, the vertex resolution is dominated by multiple Coulomb scattering. This imposes strict constraints on the design of the detector. In particular, the innermost layer of the *vertex detector* must be placed as close to the interaction point as possible, the support structure must be low in mass but rigid, and the readout electronics must be placed outside of the tracking volume. The design must also withstand a large beam background which exceeds 200 krad/year (2 kGy/year). Radiation doses of this level both cause high noise in the electronics and lead to an increase of leakage currents in the silicon detectors. In addition, the beam background induces large single-hit counting rates. The electronic shaping time (currently set to 500 ns) is determined by a trade-off between the desire to minimise counting-rate and leakage-current effects, which argue for short shaping times, and input-FET noise of front-end integrated circuits, which is minimised with longer shaping times (see also Chap. 14).

Since 1999, several versions of the SVD were exploited [3]. The present detector, SVD-2.0 [4], is shown in Fig. 13.2. It consists of four layers in a

https://doi.org/10.1017/9781009401531.016 Published online by Cambridge University Press

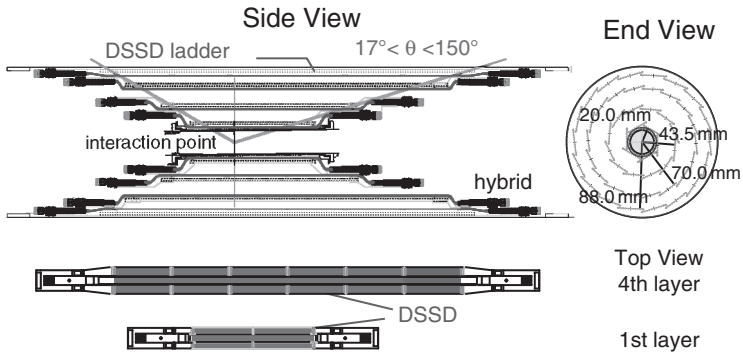

Fig. 13.2. Silicon vertex detector SVD-2.0.

barrel-only design and covers a polar angle of $17° < \theta < 150°$. Each layer is constructed of independent ladders. The ladders comprise *double-sided silicon strip detectors* (DSSDs) reinforced by boron-nitride support ribs.

The double-sided silicon strip detector used in the present SVD is an S4387 microstrip detector manufactured by Hamamatsu Photonics especially for Belle. The thickness of the depleted area is 300 µm, the bias potentials applied to p and n sides are -40 V and $+40$ V, respectively. Strip pitches are 75 µm for the p side, which is used for the z-coordinate measurement, and 50 µm for the n side that measures φ. The total number of readout channels is 110 592.

The readout chain for this detector is based on the VA1TA integrated circuit which is placed to the ceramic hybrid and connected to the DSSD [5]. The VA1TA chip is manufactured using 0.35 µm basic-size elements. It comprises 128 readout channels. The small size of the elements provides good radiation tolerance. Each channel contains a charge-sensitive preamplifier followed by a CR–RC shaping amplifier. The outputs of the shapers are fed to track and hold circuits, which consist of capacitors and CMOS switches. The trigger signal initiates the analogue information to be transferred to storage capacitors which then can be sequentially read out. The important feature of this chip is its excellent radiation tolerance of more than 20 Mrad (200 kGy).

The back-end electronics is a system of flash analogue-to-digital converters (FADCs), digital signal processors (DSPs) and field-programmable gate arrays (FPGAs), mounted on standard 6U VME boards. The digital signal processors perform on-line common-mode noise subtraction, data sparsification and data formatting.

The impact-parameter resolution depending on the particle momentum is presented in Fig. 13.3. The resolution of the present silicon vertex detector is approximated by the formulae

https://doi.org/10.1017/9781009401531.016 Published online by Cambridge University Press

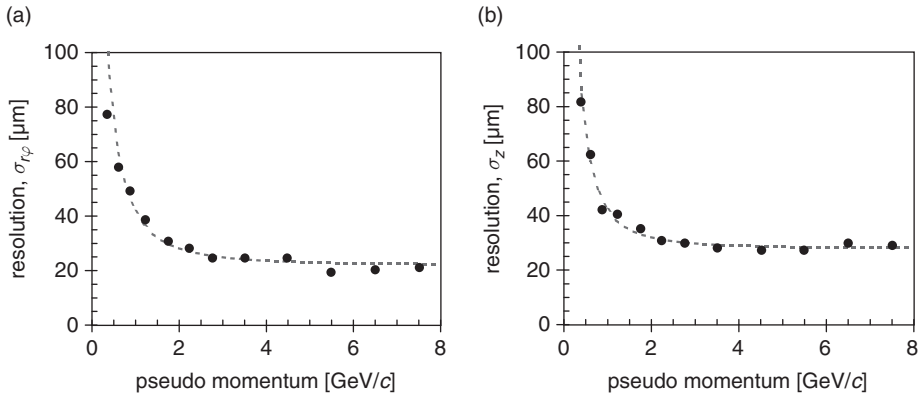

Fig. 13.3. Impact-parameter resolution depending on the particle momentum for the '$r\varphi$' projection (a) and in the 'z' coordinate (b). The measurement was performed with cosmic-ray muons. The dashed lines are approximations according to the quoted formulae. The 'pseudo momentum' is $p\beta \sin^{3/2}\theta$ for the $r\varphi$ projection and $p\beta \sin^{5/2}\theta$ for the z projection.

$$\sigma_{r\varphi}\ [\mu\mathrm{m}] = \sqrt{(22)^2 + \left(\frac{36}{p\ [\mathrm{GeV}/c]\,\beta\,\sin^{3/2}\theta}\right)^2}\ , \tag{13.1}$$

$$\sigma_{z}\ [\mu\mathrm{m}] = \sqrt{(28)^2 + \left(\frac{32}{p\ [\mathrm{GeV}/c]\,\beta\,\sin^{5/2}\theta}\right)^2}\ . \tag{13.2}$$

13.1.2 The central drift chamber (CDC)

The *CDC* geometry can be seen in Fig. 13.1 [6]. It is asymmetric in the z direction in order to provide an angular coverage of $17° < \theta < 150°$. The longest wires are 2400 mm long. The inner and outer CDC radii are 102 mm and 874 mm, respectively. The forward and backward small-r regions have conical shapes in order to get clear of the accelerator components while maximising the acceptance.

The chamber has 50 cylindrical layers of anode wires and 8400 drift cells that are organised into 6 axial and 5 small-angle stereo superlayers. The stereo angles in each stereo superlayer are determined by maximising the z measurement capability while keeping the gain variations along the wire below 10%. Thus, the stereo angles vary from −57 mrad to +74 mrad.

The individual drift cells are nearly quadratic and, except for the inner two layers, have a maximum drift distance between 8 mm and 10 mm and a

https://doi.org/10.1017/9781009401531.016 Published online by Cambridge University Press

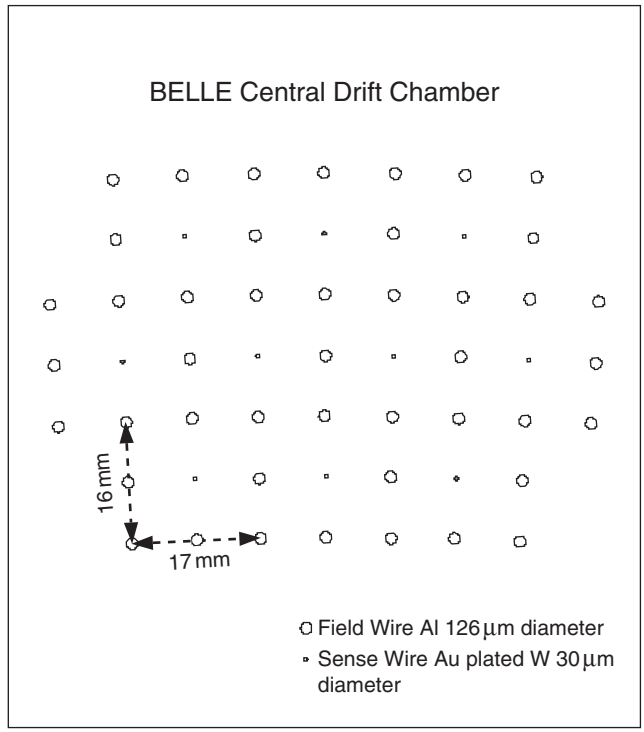

Fig. 13.4. The Belle CDC cell structure.

radial width that ranges from 15.5 mm to 17 mm (Fig. 13.4). The drift cells in the inner layers are smaller than the others having sizes about 5 mm × 5 mm. The sense wires are gold-plated tungsten wires of 30 μm diameter to maximise the electric drift field. To reduce the material, the field wires are made of unplated aluminium. The 126 μm diameter was chosen to keep the electric field on the surface of the wires below 20 kV/cm, the limit for avoiding radiation damage (see Chap. 12). The total wire tension of 3.5 tons is supported by aluminium end plates and carbon-fibre-reinforced-plate (CFRP) cylinder structures that extend between the end plates.

The use of a low-Z gas is important for minimising multiple-Coulomb-scattering contributions to the momentum resolution. Since low-Z gases have a smaller photoelectric cross section than argon-based gases, they have the additional advantage of reduced background from synchrotron radiation. A gas mixture of 50% helium and 50% ethane was selected for the CDC filling. This mixture has a long radiation length (640 m), and a drift velocity that saturates at 4 cm/μs at a relatively low electric field [7, 8]. This is important for operating square-cell drift chambers because of large field non-uniformities inherent to their geometry. The use

https://doi.org/10.1017/9781009401531.016 Published online by Cambridge University Press

of a saturated gas makes calibration simpler and helps to ensure reliable and stable performance. Even though the gas mixture has a low Z, a good $\mathrm{d}E/\mathrm{d}x$ resolution is provided by the large ethane component [9].

The CDC electronics is described in [10]. Signals are amplified by Radeka-type preamplifiers placed inside the detector, and then sent to Shaper–Discriminator–QTC modules (charge(Q)-to-Time Conversion) in the electronics hut via $\approx$ 30 m long twisted-pair cables. This module receives, shapes and discriminates signals, and performs a charge(Q)-to-time(T) conversion. The module internally generates a logic-level output, where the leading edge determines the drift time and the width is proportional to the input pulse height. This technique is a rather simple extension of the ordinary TDC/ADC readout scheme, but allows to use only TDCs to measure both the timing and charge of the signals. Since multihit TDCs operate in the common stop mode, one does not need a long delay that analogue signals usually require in an ADC readout with a gate produced by a trigger signal.

The spatial resolution as a function of the drift distance, measured with cosmic rays, is shown in Fig. 13.5. For tracks passing near the centre of the drift space it is better than 100 μm. The momentum resolution as a function of transverse momentum p_T measured with cosmic muons is approximated by the formula

$$\frac{\sigma_{p_\mathrm{T}}}{p_\mathrm{T}}[\%] = \sqrt{((0.201 \pm 0.003) p_\mathrm{T}\ [\mathrm{GeV}/c])^2 + ((0.290 \pm 0.006)/\beta)^2}\ . \tag{13.3}$$

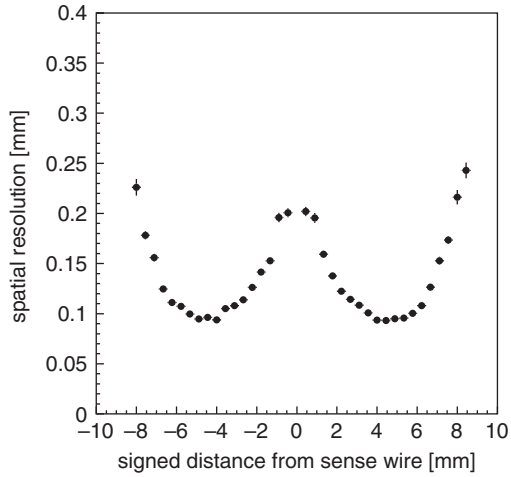

Fig. 13.5. Spatial resolution as a function of the drift distance.

https://doi.org/10.1017/9781009401531.016 Published online by Cambridge University Press

No apparent systematic effects due to different particle charge were observed. The momentum resolution measured in the experiment for muons produced in the process $e^+e^- \to \mu^+\mu^-$ is $\sigma_{p_T}/p_T = (1.64 \pm 0.04)\%$ for the momentum range 4–5.2 GeV/c. This is somewhat worse compared to the Monte Carlo expectations.

The $\mathrm{d}E/\mathrm{d}x$ measurements in the central drift chamber are used for particle identification. The truncated-mean method was employed to estimate the most probable energy loss. The largest 20% of the measured $\mathrm{d}E/\mathrm{d}x$ values for each track were discarded and the remaining data were averaged. Such a procedure minimises an influence of the tail of the $\mathrm{d}E/\mathrm{d}x$ Landau distribution. The $\langle \mathrm{d}E/\mathrm{d}x \rangle$ resolution was measured to be 7.8% in the momentum range from 0.4 GeV/c to 0.6 GeV/c, while the resolution for Bhabha and μ-pair events is about 6%.

13.1.3 The aerogel Cherenkov-counter system (ACC)

Particle identification, specifically the ability to distinguish $\pi^\pm$ from $K^\pm$, plays a key rôle in the understanding of CP violation in the B system. An array of silica-aerogel threshold Cherenkov counters has been selected as part of the Belle particle-identification system to extend the momentum coverage beyond the reach of $\mathrm{d}E/\mathrm{d}x$ measurements by the CDC and by time-of-flight measurements by the time-of-flight system (TOF).

The configuration of the *silica-aerogel Cherenkov-counter system* (ACC), in the central part of the Belle detector, is shown in Fig. 13.6 [11, 12]. The ACC consists of 960 counter modules segmented into 60 cells in the φ direction for the barrel part and 228 modules arranged in 5

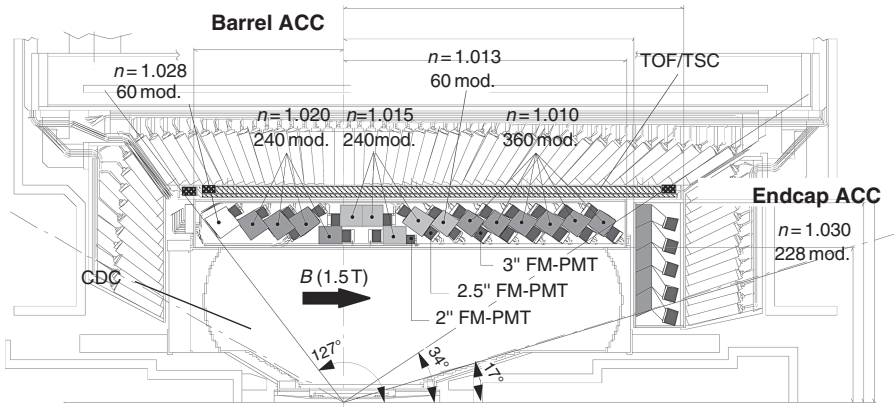

Fig. 13.6. The arrangement of the ACC system.

https://doi.org/10.1017/9781009401531.016 Published online by Cambridge University Press

concentric layers for the forward endcap part of the detector. All counters are arranged in a projective semi-tower geometry, pointing to the interaction point. In order to obtain good pion/kaon separation for the whole kinematical range, the refractive indices of the aerogels are selected to be between 1.01 and 1.03, depending on their polar-angle region.

The counter contains five aerogel tiles stacked in a thin (0.2 mm thick) aluminium box of approximate dimensions $12\times12\times12\,\mathrm{cm}^3$. Since the ACC is operated in a high magnetic field of 1.5 T in the Belle detector, *fine-mesh photomultiplier tubes* (FM PMTs), attached directly to the aerogels at the sides of the box, are used for the detection of Cherenkov light, taking advantage of their large effective area and high gain [13].

Silica aerogel has been used in several experiments, but its transparency became worse within a few years of use. This phenomenon may be attributed to the hydrophilic property of silica aerogel. In order to prevent such effects, a special type of this material was developed and produced, highly hydrophobic by changing the surface hydroxyl groups into trimethylsilyl groups [14]. As a result of this treatment, the silica aerogel used for the Belle's ACC remains transparent even four years after it has been manufactured.

All aerogel tiles thus produced have been checked for optical transparency, transmittance of unscattered light, refractive index, dimensions, etc.

The FM PMTs were produced by Hamamatsu Photonics. Each FM PMT has a borosilicate glass window, a bialkali photocathode, 19 fine-mesh dynodes and an anode. Three types of FM PMTs of 2, 2.5 and 3 inches in diameter are used in the ACC. The average quantum efficiency of the photocathode is 25% at 400 nm wavelength. The optical acceptance, that is, the ratio of the total area of the holes to the total area of mesh dynodes is about 50%.

The FM PMTs with 19 dynode stages of fine mesh have high gain ($\approx 10^8$) at moderate HV values (< 2500 V). The gain of the FM PMT decreases as a function of the magnetic field strength. The gain reduction factor is about 200 at 1.5 T for FM PMTs placed parallel to the direction of the magnetic field and it slightly recovers when they are tilted.

The performance of the ACC system is illustrated by Fig. 13.7 that shows the measured pulse-height distribution for the barrel ACC for $e^{\pm}$ tracks in Bhabha events and also $K^{\pm}$ candidates in hadronic events, which are selected by time-of-flight and $\mathrm{d}E/\mathrm{d}x$ measurements [15]. The figure demonstrates a clear separation between high-energy electrons and below-threshold particles. It also indicates good agreement between the data and a Monte Carlo simulation [16].

https://doi.org/10.1017/9781009401531.016 Published online by Cambridge University Press

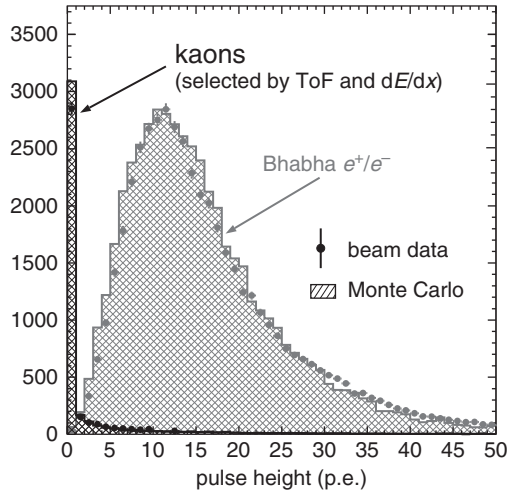

Fig. 13.7. Pulse-height spectra in units of photoelectrons observed by the barrel ACC for electrons and kaons. Kaon candidates were obtained by $\mathrm{d}E/\mathrm{d}x$ and TOF measurements. The Monte Carlo expectations are superimposed.

13.1.4 Time-of-flight counters (TOF)

For a 1.2 m path, the *TOF system* with 100 ps time resolution is effective for particle momenta below about 1.2 GeV/c, which encompasses 90% of the particles produced in $\Upsilon(4S)$ decays. In addition to particle identification, the TOF counters provide fast signals for the trigger system to generate gate signals for ADCs and stop signals for TDCs.

The TOF system consists of 128 TOF counters and 64 thin trigger scintillation counters (TSCs). Two trapezoidally shaped TOF counters and one TSC counter, with a 1.5 cm intervening radial gap, form one module. In total 64 TOF/TSC modules located at a radius of 1.2 m from the interaction point cover a polar-angle range from 34° to 120°. The minimum transverse momentum to reach the TOF counters is about 0.28 GeV/c. The module dimensions are given in Fig. 13.8. These modules are individually mounted on the inner wall of the barrel ECL container. The 1.5 cm gap between the TOF counters and TSC counters was introduced to isolate the time-of-flight system from photon-conversion backgrounds by requiring a coincidence between the TOF and TSC counters. Electrons and positrons created in the TSC layer are prevented from reaching the TOF counters due to spiralling in this gap in the 1.5 T field.

Hamamatsu (HPK) type R6680 fine-mesh photomultipliers (FM PMTs), with 2 inch diameter and 24 dynode stages, have been selected for the TOF counter. These FM PMTs provide a gain of 3×10^6 at a high voltage below 2800 V in a magnetic field of 1.5 T. The bialkali photocathode

https://doi.org/10.1017/9781009401531.016 Published online by Cambridge University Press

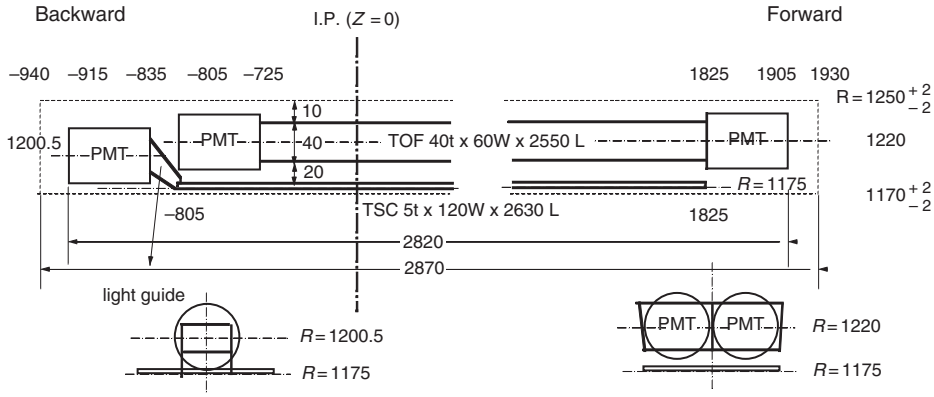

Fig. 13.8. Layout of the Belle TOF system.

with an effective diameter of 39 mm covers 50% of the end area of each TOF counter. The transit-time spread is 320 ps (rms), the rise and fall times are 3.5 ns and 4.5 ns, respectively, and the pulse width is about 6 ns at FWHM. FM PMTs were attached to the TOF counter ends with an air gap of ≈ 0.1 mm. In the case of the TSC counters the tubes were glued to the light guides at the backward ends. The air gap between the scintillator and PMT in the TOF counter helps to select earlier-arrival photons and reduces the gain-saturation effect of the FM PMT that might arise due to large pulses at a very high rate. Photons arriving at large angles to the counter axis cannot leave the scintillator due to internal reflection and reach the PMT. In this way only photons with shorter travel times and smaller time spread are selected.

The TOF and TSC scintillators (BC408, Bicron) were wrapped with one layer of 45 μm thick polyvinyl film (Tedlar) for light tightness and surface protection. This thin wrapping minimises the dead space between adjacent TOF counters. The effective light attenuation length is about 3.9 m while the effective light propagation velocity is 14.4 cm/ns. The number of photoelectrons received from the TSC counter per one minimum-ionising particle (MIP) crossing the counter depends considerably on the crossing point of the particle, but it exceeds 25 photoelectrons over the whole counter. This ensures a high efficiency of 98% for the TOF trigger even at a nominal discrimination level of 0.5 MIPs.

A block diagram of a single channel of the TOF front-end electronics is shown in Fig. 13.9. Each photomultiplier signal is split into two. One is sent to the charge-to-time converter and then to a multihit TDC for charge measurement. The other generates signals corresponding to two different threshold levels: a high level (HL) and a low level (LL). Two LeCroy MVL107s (Monolithic Voltage Comparators) are used for discriminators,

https://doi.org/10.1017/9781009401531.016 Published online by Cambridge University Press

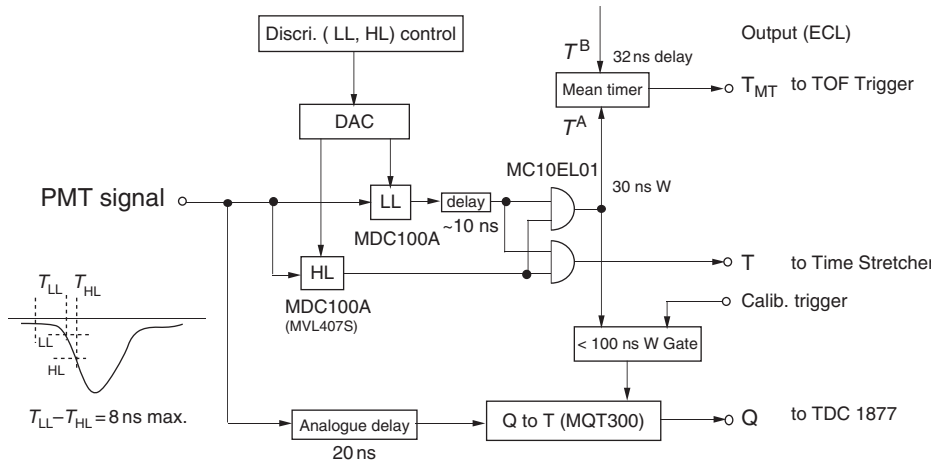

Fig. 13.9. Block diagram of a single channel of the TOF front-end electronics.

with threshold levels set between 0.3–0.5 MIPs for HL and 0.05–0.1 MIPs for LL. The LL output provides the TOF timing and the HL output provides a trigger signal. The HL is used to generate a self gate for the LeCroy MQT300A Q-to-T conversion and also to gate the LL output. A common trigger is prepared for pedestal calibration of the MQT300A. The signal T is further processed in a time stretcher for readout by a TDC 1877S. The MQT (monolithic charge-to-time converter) output Q is a timing signal corresponding to the charge, which is directly recorded with the TDC 1877S.

To achieve high time resolution the following time-walk correction formulae are applied in the off-line data processing:

$$T_{\rm obs}^{\rm twc} = T_{\rm raw} - \left(\frac{z}{V_{\rm eff}} + \frac{S}{\sqrt{Q}} + F(z) \right) \ , \tag{13.4}$$

where $T_{\rm raw}$ is the PMT signal time, z is the particle's hit position on a TOF counter, $V_{\rm eff}$ is the effective velocity of light in the scintillator, Q is the charge of the signal, S is the coefficient of time walk, $T_{\rm obs}^{\rm twc}$ the time-walk-corrected observed time, and

$$F(z) = \sum_{n=0}^{n=5} A_n z^n \ . \tag{13.5}$$

The coefficients, $1/V_{\rm eff}$, S and A_n for $n = 0$ to 5, were determined from experimental data.

https://doi.org/10.1017/9781009401531.016 Published online by Cambridge University Press

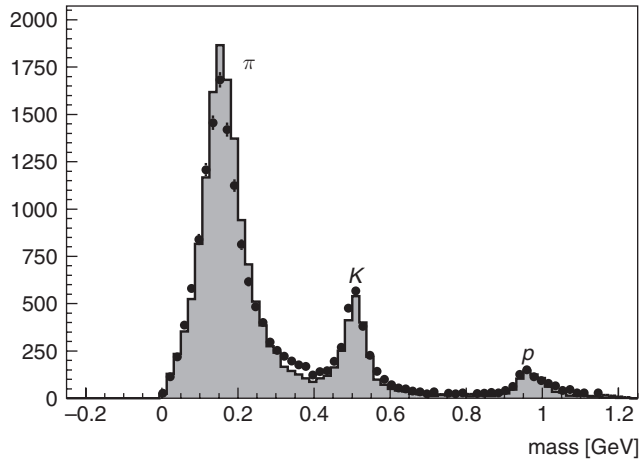

Fig. 13.10. Mass distribution from TOF measurements for particle momenta below 1.2 GeV/c.

The counter time resolution measured for muons from the process $e^+e^- \to \mu^+\mu^-$ is about 100 ps with a small z dependence. This satisfies the design goal. This value is reached even though the transit-time spread is 320 ps, because the number of photoelectrons is about 200 per minimum-ionising particle. Therefore – due to large photoelectron statistics – the contribution of the transit-time spread to the time resolution is considerably reduced. Figure 13.10 shows the mass distribution for tracks with momenta below 1.2 GeV/c in hadronic events. The mass m is calculated using the equation

$$m^2 = \left(\frac{1}{\beta^2} - 1\right) P^2 = \left[\left(\frac{cT_{\rm obs}^{\rm twc}}{L_{\rm path}}\right)^2 - 1\right] P^2 \ , \qquad (13.6)$$

where P and $L_{\rm path}$ are the momentum and path length of the particle determined from the CDC track fit. Clear peaks corresponding to $\pi^\pm, K^\pm$ and protons are seen. The data points are in good agreement with a Monte Carlo prediction (histogram) of $\sigma_{\rm TOF} = 100$ ps.

13.1.5 Electromagnetic calorimetry (ECL)

Since one third of B decay products are π^0s and other neutral particles providing photons in a wide range from 20 MeV to 4 GeV, a *high-resolution calorimeter* is a very important part of the detector. CsI(Tl) scintillation crystals were chosen as a material for the calorimeter due to the high CsI(Tl) light output, its short radiation length, good mechanical properties and moderate price. The main tasks of the calorimeter are:

https://doi.org/10.1017/9781009401531.016 Published online by Cambridge University Press

- detection of γ quanta with high efficiency,
- precise determination of the photon energy and coordinates,
- electron/hadron separation,
- generation of a proper signal for the trigger,
- on-line and off-line luminosity measurement.

The electromagnetic calorimeter (ECL) consists of a barrel section of 3.0 m in length with an inner radius of 1.25 m and annular endcaps at $z = 2.0$ m (forward part) and $z = -1.0$ m (backward part) from the interaction point. The calorimeter covers the polar-angle region of $12.4^\circ < \theta < 155.1^\circ$ except for two gaps $\approx 1^\circ$ wide between the barrel and endcaps.

The barrel part has a tower structure projected to the vicinity of the interaction point. It contains 6624 CsI(Tl) modules of 29 different types. Each crystal is a truncated pyramid of average size of about $6 \times 6\,\mathrm{cm}^2$ in cross section and 30 cm ($16.2\,X_0$) in length. The endcaps contain altogether 2112 CsI crystals of 69 types. The total number of the crystals is 8736 with a total mass of about 43 tons.

Each crystal is wrapped with a layer of 200 μm thick Gore-Tex porous Teflon and covered by a 50 μm thick aluminised polyethylene. For light readout two $10 \times 20\,\mathrm{mm}^2$ Hamamatsu S2744-08 photodiodes are glued to the rear surface of the crystal via an intervening 1 mm thick acrylic plate. The acrylic plate is used because direct glue joints between the photodiode and the CsI were found to fail after temperature cycling, probably due to the different thermal expansion coefficients of silicon and CsI. The LED attached to the plate can inject light pulses to the crystal volume to monitor the stability of the optical condition. Two preamplifiers are attached to the photodiodes. For electronic channel monitoring and control, test pulses are fed to the inputs of the preamplifier. An aluminium-shielded preamplifier box is attached to the aluminium base plate with screws. The mechanical assembly of a single CsI(Tl) counter is shown in Fig. 13.11. The signal yield of this counter was measured to be about 5000 photoelectrons per 1 MeV of energy deposited in the crystal. The noise level is equal to about 200 keV in absence of a beam.

The barrel crystals were installed in a honeycomb-like structure formed by 0.5 mm-thick aluminium septum walls stretched between the inner and outer cylinders. The outer cylinder, the two end rings and the reinforcing bars are made of stainless steel and form a rigid structure that supports the weight of the crystals. The inner cylinder is made of 1.6 mm-thick aluminium to minimise the inactive material in front of the calorimeter. The overall support structure is made gas tight and filled with dry air to provide a low-humidity (5%) environment for the CsI(Tl)

https://doi.org/10.1017/9781009401531.016 Published online by Cambridge University Press

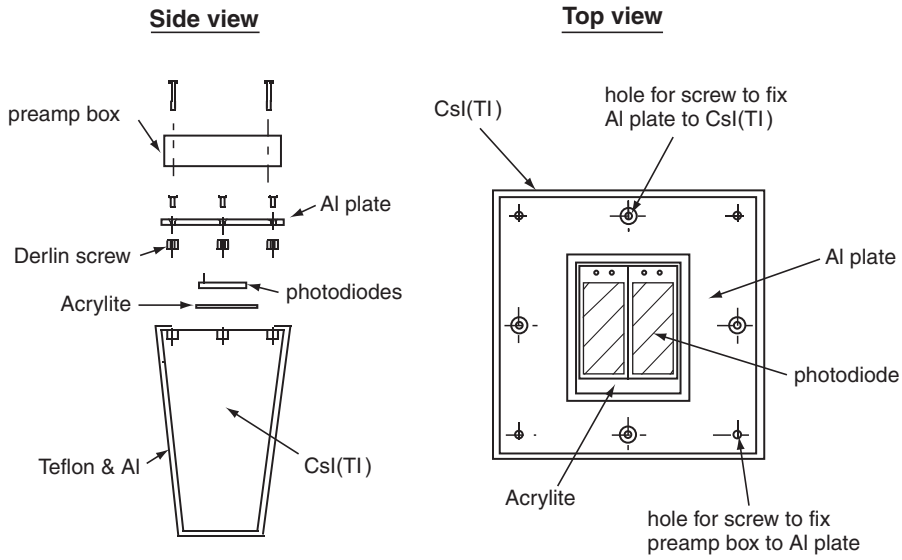

Fig. 13.11. Mechanical assembly of the ECL counter.

crystals. The preamplifier heat, a total of 3 kW, is removed by a liquid-based cooling system. An operating temperature of lower than 30 °C with ±1 °C stability is required for the stable operation of the electronics. The endcap support structure is similar to that of the barrel.

A block diagram of the readout electronics is shown in Fig. 13.12. The preamplifier output is transmitted by 10 m long, 50 Ω twisted-pair cables to a shaping circuit where the two signals from the same crystal are summed. The summed signal is then split into two streams: one for the main data acquisition for energy measurements and the other for the trigger electronics. The main signals for energy measurements are shaped with a $\tau = 1\,\mu$s time constant and fed into a charge-to-time (Q-to-T) converter, LeCroy MQT300A, installed on the same card. The output of the Q-to-T converter is transmitted via a twisted pair to a multi-hit TDC module (LeCroy 1877S) in the electronics hut for digitisation. The trigger signal is shaped with a shorter time constant and ≈ 16 lines are combined to form an analogue sum for the level-1 trigger.

The absolute energy calibration has been carried out by using Bhabha ($e^+e^- \to e^+e^-$) and annihilation ($e^+e^- \to \gamma\gamma$) events. With a sample containing $N_{e^+e^-}$ Bhabha events, the calibration constant of the jth counter g_j is obtained by minimising χ^2 defined as

$$\chi^2 = \sum_k^{2N_{e^+e^-}} \left(\frac{E_k(\theta) f(\theta) - \sum_j g_j E_j}{\sigma} \right)^2 , \qquad (13.7)$$

https://doi.org/10.1017/9781009401531.016 Published online by Cambridge University Press

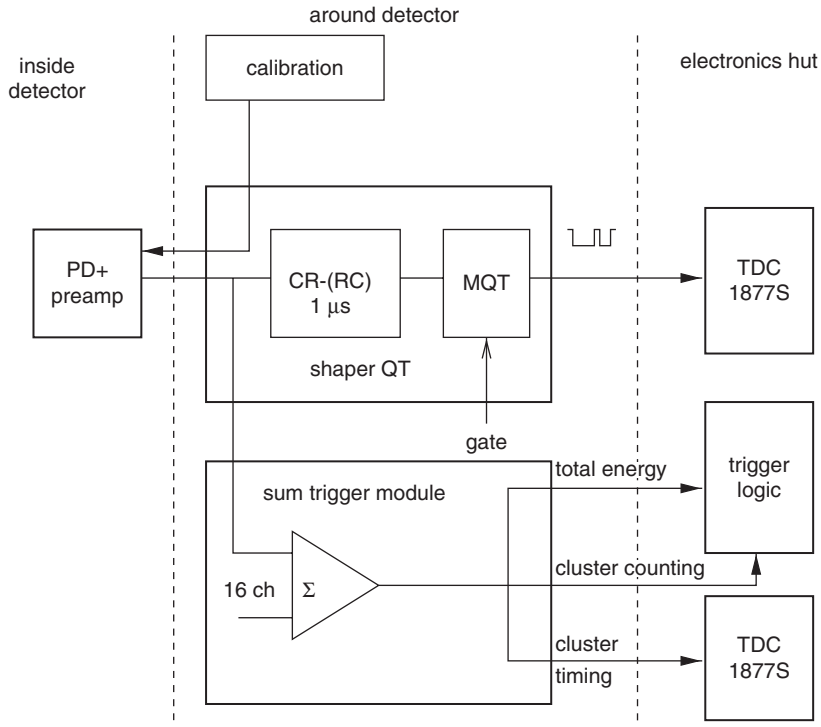

Fig. 13.12. Block diagram of the ECL readout electronics.

where E_k is the expected energy of the scattered electrons. All electrons and positrons are included in the sum. This value is a function of θ in the asymmetric collider. The function $f(\theta)$ is the correction factor due to shower leakage and the effect of the front material, which was determined by a Monte Carlo simulation. The χ^2 minimisation is carried out by taking a $\approx 8000 \times 8000$ sparse-matrix inversion into account. Approximately 100 events per counter are used for this calibration.

An energy resolution for electrons of about 1.7% for the energy range from 4 GeV to 7 GeV was achieved from Bhabha scattering ($e^+e^- \rightarrow e^+e^-$) averaged over the whole calorimeter as shown in Fig. 13.13. The resolution does not change too much in this energy region since the leakage of the calorimeter increases with energy while the number of particles in the shower is also increasing and these effects compensate each other up to certain extent.

Two-photon invariant-mass distributions in hadronic events are shown in Figs. 13.14 (a) and (b). The clear peaks of π^0 and η mesons are seen at each nominal mass, and a mass resolution has been achieved to be 4.8 MeV for π^0 and about 12 MeV for η.

https://doi.org/10.1017/9781009401531.016 Published online by Cambridge University Press

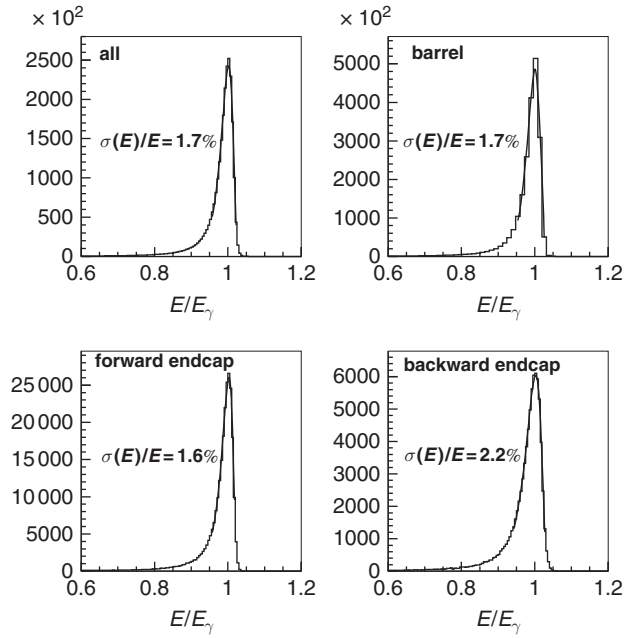

Fig. 13.13. Energy resolutions measured from Bhabha event samples: overall, barrel, forward endcap and backward endcap.

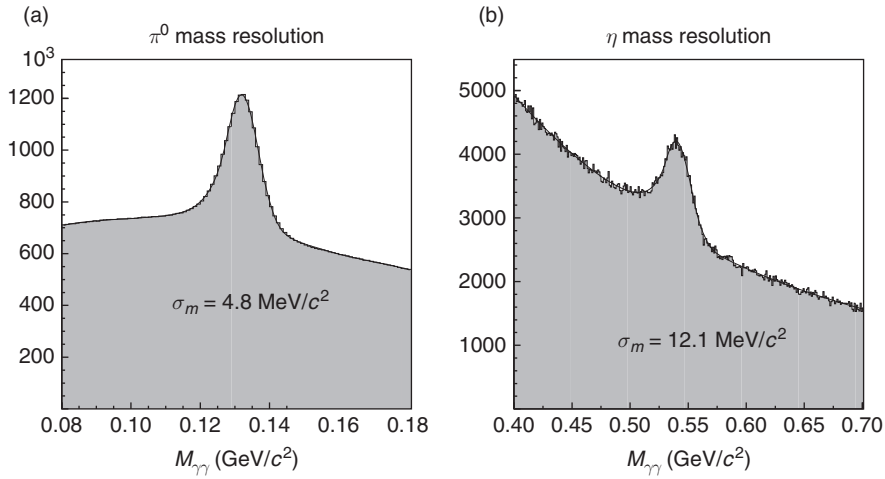

Fig. 13.14. Two-photon invariant-mass distribution for hadronic events (a) in the $\pi^0 \to \gamma\gamma$ and (b) the $\eta \to \gamma\gamma$ range, where each photon energy was required to be greater than 30 MeV in the barrel region.

https://doi.org/10.1017/9781009401531.016 Published online by Cambridge University Press

13.1.6 The K_L and muon detection system (KLM)

The *KLM detection system* was designed to identify K_{L}s and muons with high efficiency over a broad momentum range greater than $600\,\mathrm{MeV}/c$. The barrel-shaped region around the interaction point covers an angular range from 45° to 125° in polar angle, and the endcaps in the forward and backward directions extend this range to 20° and 155°.

The KLM detection system consists of alternating layers of charged-particle detectors and 4.7 cm-thick iron plates. There are 15 detector layers and 14 iron layers in the octagonal barrel region and 14 detector layers in each of the forward and backward endcaps. The iron plates provide a total of 3.9 interaction lengths of material for a particle travelling normal to the detector planes. In addition, the electromagnetic calorimeter, ECL, provides another 0.8 interaction length of material to convert K_{L}s. K_{L}s which interact in the iron or ECL produce a shower of ionising particles. The location of this shower determines the direction of the K_{L}, but the size of the shower does not permit a useful measurement of the K_{L} energy. The multiple layers of charged-particle detectors and iron allow a discrimination between muons and charged hadrons ($\pi^{\pm}$ or $K^{\pm}$) based upon their range and transverse scattering. Muons pass a much longer distance with smaller deflections on average than strongly interacting hadrons.

Charged particles are detected in the KLM system by glass–electrode resistive-plate counters (RPCs) [17, 18]. Resistive-plate counters have two parallel plate electrodes with high bulk resistivity ($\geq 10^{10}\,\Omega \cdot \mathrm{cm}$) separated by a gas-filled gap. In the streamer mode, an ionising particle traversing the gap initiates a streamer in the gas that results in a local discharge of the plates. The discharge induces a signal on external pickup strips, which is used to record the location and the time of the ionisation.

Figure 13.15 shows the cross section of a superlayer, in which two RPCs are sandwiched between the orthogonal θ and φ pickup strips with ground planes for signal reference and proper impedance. This unit structure of two RPCs and two readout planes is enclosed in an aluminium box and is less than 3.7 cm thick. Signals from both RPCs are picked up by copper strips above and below the pair of RPCs, providing a three-dimensional space point for particle tracking. Multiple scattering of particles as they travel through the iron is typically a few centimetres. This sets the scale for the projected spatial resolution of the KLM. The pickup strips in the barrel vary in width from layer to layer but are approximately 50 mm wide with lengths from 1.5 m to 2.7 m.

The double-gap design provides redundancy and results in high superlayer efficiency of $\geq 98\%$, despite the relatively low single-layer RPC efficiency of 90% to 95%.

https://doi.org/10.1017/9781009401531.016 Published online by Cambridge University Press

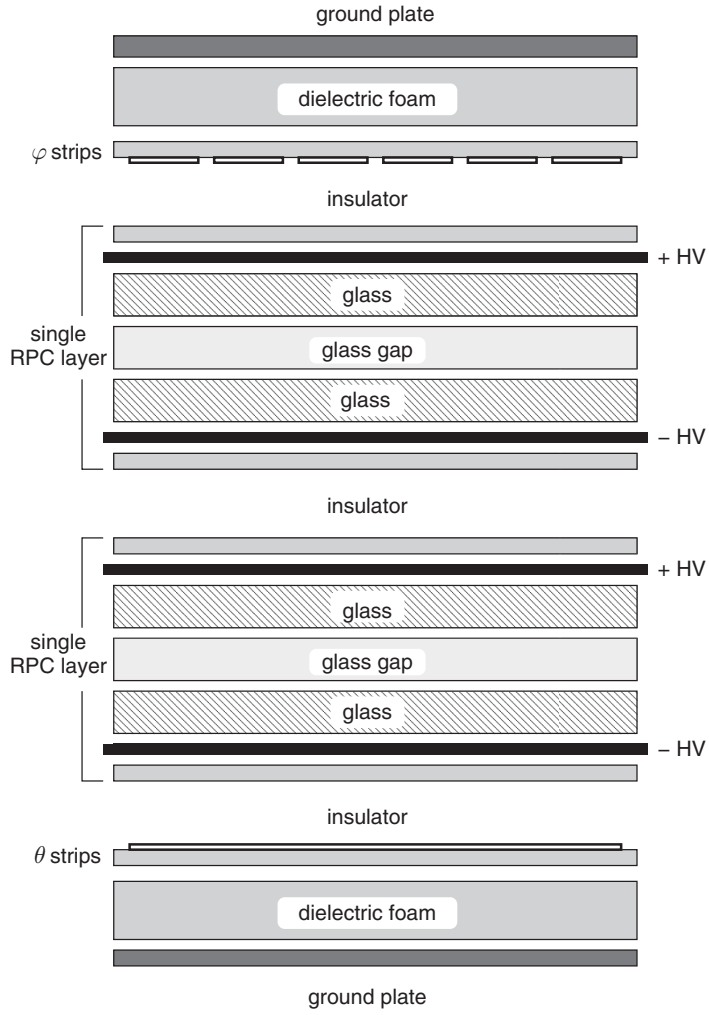

Fig. 13.15. Cross section of a KLM superlayer.

Cosmic rays were used to measure the detection efficiency and resolution of the superlayers. The momenta of cosmic muons were measured by the central drift chamber using the solenoidal field of 1.5 T. Below 500 MeV/c, the muons do not reach the KLM system. A comparison of the measured range of a particle with the predicted range for a muon allows us to assign a likelihood of being a muon. In Fig. 13.16a the muon detection efficiency versus momentum is shown for a likelihood cut of 0.7. Some fraction of charged pions and kaons will be misidentified as muons. A sample of $K_S \to \pi^+\pi^-$ events in the e^+e^- collision data was used to determine this fake rate. The fraction of pions which is misidentified as

https://doi.org/10.1017/9781009401531.016 Published online by Cambridge University Press

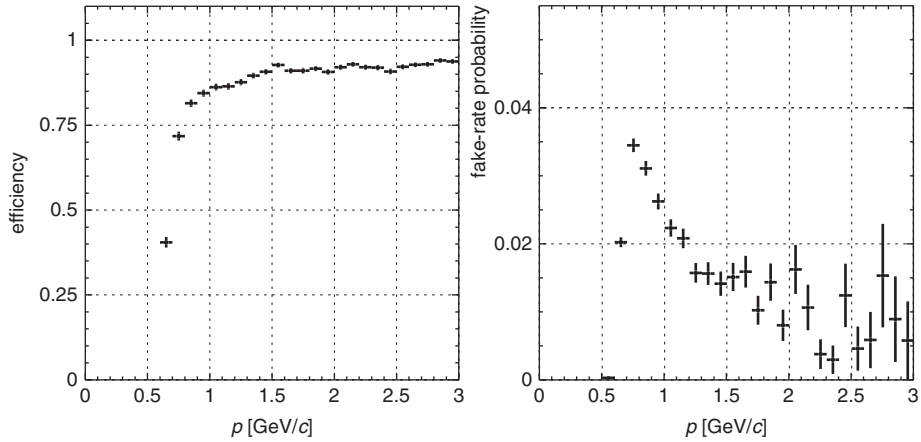

Fig. 13.16. Muon detection efficiency (a) and fake-rate probability (b) versus momentum in the K_L and muon detection system.

muons is shown in Fig. 13.16b again with the same muon likelihood cut. Above 1.5 GeV/c one finds a muon-identification efficiency of better than 90% with a fake-rate probability of less than 2%.

13.2 Particle identification

For *particle identification* at the Belle detector the information from all subsystems is used.

Electrons are identified by using the following discriminants:

- the ratio of energy deposited in the electromagnetic calorimeter (ECL) and charged-track momentum measured by the central drift chamber (CDC),
- the transverse shower shape in the ECL,
- the matching between a cluster in the ECL and the charged-track position extrapolated to the ECL,
- dE/dx measured by the CDC,
- the light yield in the aerogel Cherenkov-counter system (ACC), and
- time of flight measured by the time-of-flight system (TOF).

The probability density functions (PDFs) for the discriminants were formed beforehand. Based on each PDF, likelihood probabilities are calculated on a track-by-track basis and combined into a final likelihood output. This likelihood calculation is carried out by taking into account the momentum and angular dependence. The efficiency and fake-rate probability are displayed in Fig. 13.17 using electrons in real

https://doi.org/10.1017/9781009401531.016 Published online by Cambridge University Press

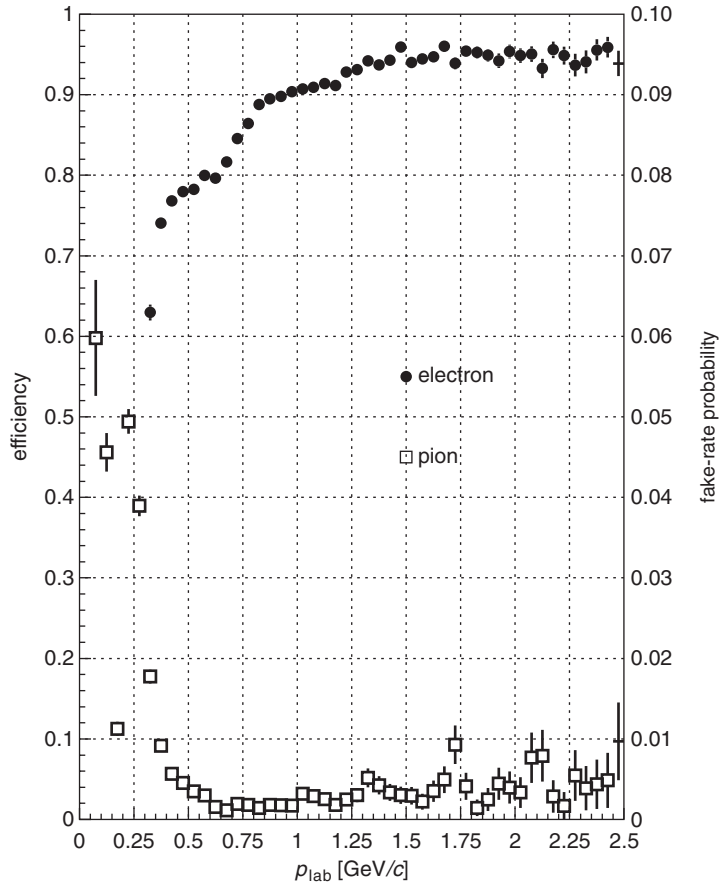

Fig. 13.17. Electron identification efficiency (circles) and fake-rate probability for charged pions (squares). Note the different scales for the efficiency and fake-rate probability.

$e^+e^- \to e^+e^-e^+e^-$ events for the efficiency measurement and $K_{\mathrm{S}} \to \pi^+\pi^-$ decays in real data for the fake-rate evaluation. For momenta greater than $1\,\mathrm{GeV}/c$, the electron identification efficiency is maintained to be above 90% while the fake-rate probability is kept at around 0.2% to 0.3%.

The K/π identification is carried out by combining information from three nearly independent measurements:

- the $\mathrm{d}E/\mathrm{d}x$ measurement by the CDC,
- the TOF measurement, and
- the measurement of the number of photoelectrons (N_{pe}) in the ACC.

https://doi.org/10.1017/9781009401531.016 Published online by Cambridge University Press

As in the case of electron identification (EID), the likelihood function for each measurement was calculated, and the product of the three likelihood functions yields the overall likelihood probability for being a kaon or a pion, P_K or P_π. A particle is then identified as a kaon or a pion by cutting on the likelihood ratio (PID):

$$\mathrm{PID}(K) = \frac{P_K}{P_K + P_\pi} \ , \quad \mathrm{PID}(\pi) = 1 - \mathrm{PID}(K) \ . \tag{13.8}$$

The validity of the K/π identification has been demonstrated using the charm decay, $D^{*+} \to D^0\pi^+$, followed by $D^0 \to K^-\pi^+$. The characteristically slow π^+ from the D^{*+} decay allows these decays to be selected with a good signal/background ratio (better than 30), without relying on particle identification. Therefore, the detector performance can be directly probed with the daughter K and π mesons from the D decay, which can be tagged by their relative charge with respect to the slow pion. The measured K efficiency and π fake-rate probability in the barrel region are plotted as functions of the track momentum from 0.5 GeV/c to 4.0 GeV/c in Fig. 13.18. A likelihood-ratio cut, $\mathrm{PID}(K) \geq 0.6$, is applied

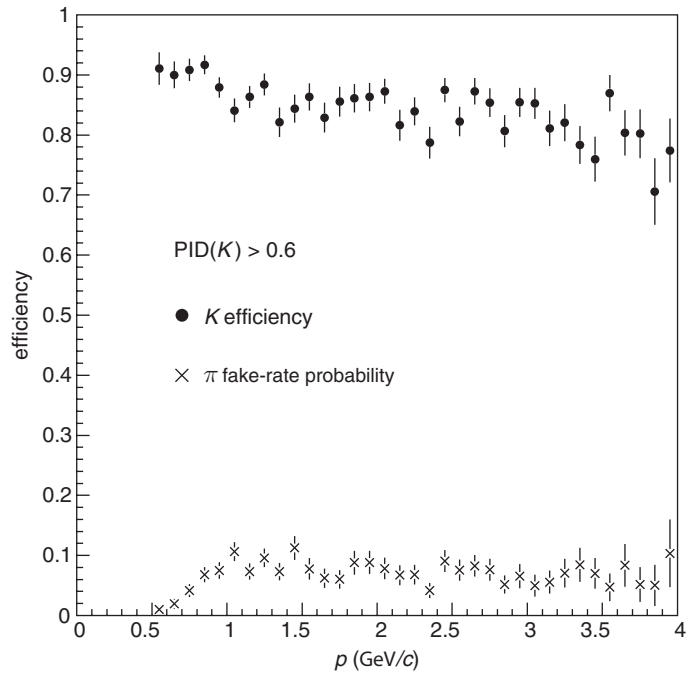

Fig. 13.18. K efficiency and π fake-rate probability, measured with $D^{\star+} \to D^0(K\pi) + \pi^+$ decays, for the barrel region. A likelihood-ratio cut $\mathrm{PID}(K) \geq 0.6$ is applied.

https://doi.org/10.1017/9781009401531.016 Published online by Cambridge University Press

in this figure. For most of the region, the measured K efficiency exceeds 80%, while the π fake-rate probability is kept below 10%.

13.3 Data-acquisition electronics and trigger system

The total rate of the physical processes of interest at a luminosity of $10^{34}\,\mathrm{cm}^{-2}\,\mathrm{s}^{-1}$ is about 100 Hz. Samples of Bhabha and $e^+e^- \to \gamma\gamma$ events are accumulated as well to measure the luminosity and to calibrate the detector responses but, since their rates are very large, these trigger rates must be prescaled by a factor of ≈ 100. Because of the high beam current, the studied events are accompanied by a high beam-related background, which is dominated by lost electrons and positrons. Thus the trigger conditions should be such that background rates are kept within the tolerance of the data-acquisition system (max. 500 Hz), while the efficiency for physics events of interest is kept high. It is important to have redundant triggers to keep the efficiency high even for varying conditions. The Belle trigger system has been designed and developed to satisfy these requirements.

The Belle *trigger system* consists of the Level-1 hardware trigger and a software trigger. Figure 13.19 shows the schematic view of the Belle Level-1 trigger system [19]. It consists of the sub-detector trigger systems and the central trigger system called the Global Decision Logic (GDL).

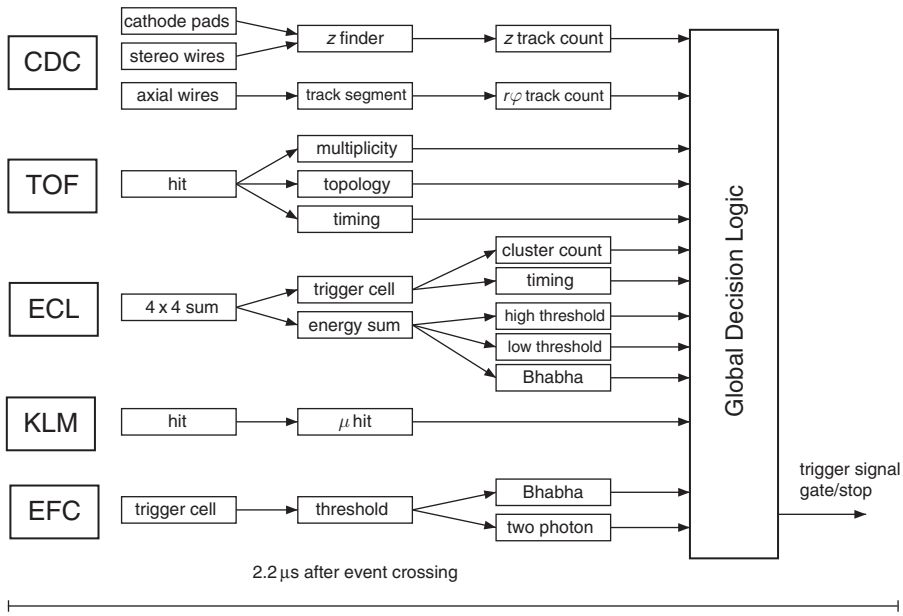

Fig. 13.19. The Level-1 trigger system for the Belle detector.

https://doi.org/10.1017/9781009401531.016 Published online by Cambridge University Press

The sub-detector trigger systems are based on two categories: track triggers and energy triggers. The central drift chamber and the time-of-flight system are used to yield trigger signals for charged particles. The CDC provides $r\varphi$- and rz-track trigger signals. The ECL trigger system provides triggers based on total energy deposit and cluster counting of crystal hits. These two categories allow sufficient redundancy. The KLM trigger gives additional information on muons. The sub-detectors process event signals in parallel and provide trigger information to the GDL, where all information is combined to characterise an event type.

The trigger system provides a trigger signal within a fixed time of 2.2 μs after the event occurrence. The trigger signal is used for the gate signal of the ECL readout and the stop signal of the TDCs for the CDC, providing T_0. Therefore, it is important to have good timing accuracy. The timing of the trigger is primarily determined by the TOF trigger which has a time jitter less than 10 ns. ECL trigger signals are also used as timing signals for events in which the TOF trigger is not available. In order to maintain the 2.2 μs latency, each sub-detector trigger signal is required to be available at the GDL input with a maximum delay of 1.85 μs. Timing adjustments are done at the input of the global decision logic. As a result, the GDL is left with a fixed 350 ns processing time to form the final trigger signal. The Belle trigger system, including most of the sub-detector trigger systems, is operated in a pipelined manner with clocks synchronised to the KEKB accelerator RF signal. The base system clock is 16 MHz which is obtained by subdividing 509 MHz RF by 32. The higher-frequency clocks, 32 MHz and 64 MHz, are also available for systems requiring faster processing.

The Belle trigger system extensively utilises programmable logic chips, Xilinx Field Programmable Gate Array (FPGA) and Complex Programmable Logic Device (CPLD) chips, which provide the majority of the trigger logic and reduce the number of types of hardware modules.

In order to satisfy the data-acquisition requirements so that it works at 500 Hz with a dead-time fraction of less than 10%, a distributed parallel system has been developed. The global scheme of the system is shown in Fig. 13.20. The entire system is segmented into seven subsystems running in parallel, each handling the data from a sub-detector. Data from each subsystem are combined into a single event record by an event builder, which converts 'detector-by-detector' parallel data streams to an 'event-by-event' data flow. The event-builder output is transferred to an on-line computer farm, where another level of event filtering is done after fast event reconstruction. The data are then sent to a mass-storage system located at the computer centre via optical fibres. A typical data size of a hadronic event by $B\bar{B}$ or $q\bar{q}$ production is measured to be about 30 kB, which corresponds to a maximum data transfer rate of 15 MB/s.

https://doi.org/10.1017/9781009401531.016 Published online by Cambridge University Press

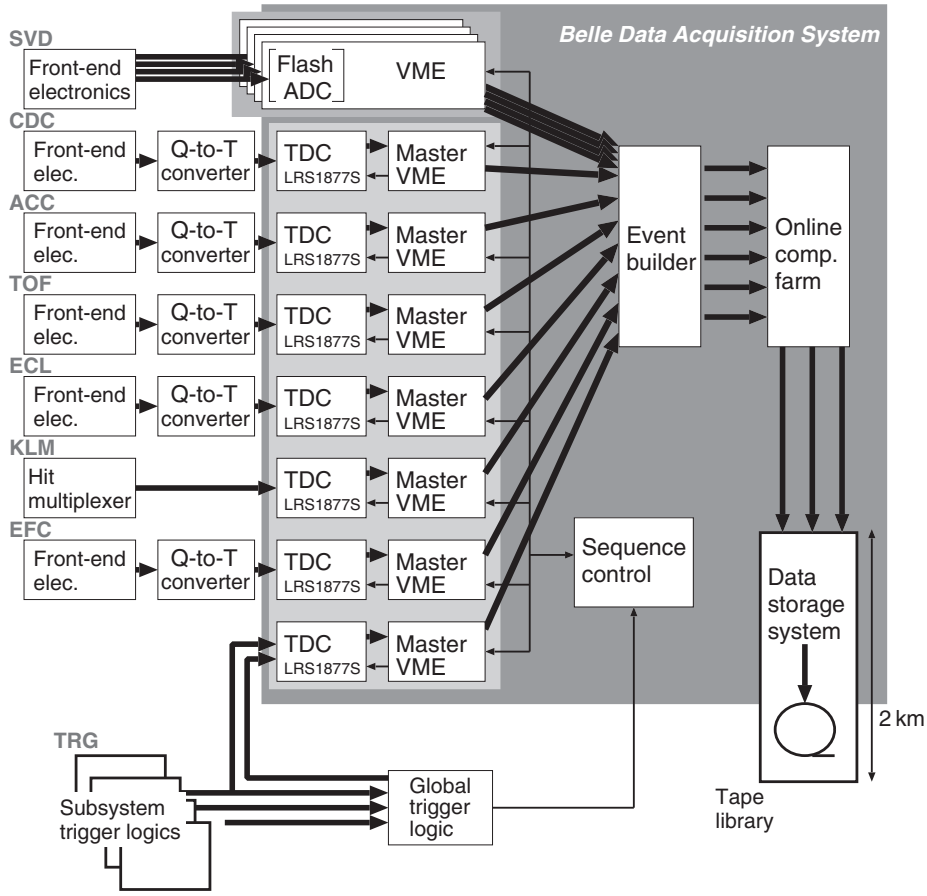

Fig. 13.20. Belle DAQ system overview.

A charge-to-time (Q-to-T) technique was adopted to read out signals from most of the detectors. Instead of using ADCs to digitise the amplitudes of signals, the charge is once stored in a capacitor and discharged at a constant rate. Two pulses, the separation of which is proportional to the signal amplitude, are generated at the start and stop moments of the discharge. By digitising the time interval of the two timing pulses with respect to a common stop timing, both the timing and the amplitude of the input signal are determined. For time digitisation a multi-hit FASTBUS TDC module, LeCroy LRS1877S, is used. Up to 16 timing pulses are recorded for 96 channels in a single-width module with a sparsification capability. The least significant bit is 500 ps. A programmable time window has a 16-bit range, which corresponds to a full scale of 32 μs.

https://doi.org/10.1017/9781009401531.016 Published online by Cambridge University Press

Most of the detectors, CDC, ACC, TOF, ECL and EFC, are read out by using the Q-to-T and TDC technique. The use of the Q-to-T technique reduces the number of cables for the CDC wires by one half. In the case of the TOF, the time resolution of 100 ps is achieved by using a time stretcher which expands the pulse width by a factor of 20. In the case of the ECL, a 16-bit dynamic range is achieved by using 3 ranges. The signal is split and fed into three preamplifiers of different gain. Then each signal feeds a Q-to-T circuit. When the signal is small, one gets four output signals: the trigger signal and three signals from the three channels. The time between each signal and the trigger is proportional to the pulse height. When the amplitude of the signal exceeds a certain value, the corresponding time exceeds a preselected gate width (overflow) and no output pulse is generated. So, for large-amplitude signals one can only see the trigger pulse and a time pulse from the low-gain channel. After digitisation one can therefore identify the analogue information by the number of time signals for the ECL pulse.

The KLM strip information is also read out by using the same type of TDC. Strip signals are multiplexed into serial lines and recorded by the TDC as time pulses. These pulses are decoded to reconstruct hit strips. Similarly, trigger signals from each subdetector including those for the intermediate stages are recorded using a TDC. A full set of trigger signals gives us complete information for the trigger studies.

A unified FASTBUS TDC readout subsystem developed for Belle is applicable to all the detectors except the Silicon Vertex Detector (SVD). A FASTBUS processor interface (FPI) controls these TDC modules, and the FPI is controlled by a readout-system controller in a master VME crate. Readout software runs on the VxWorks real-time operating system on a Motorola 68040 CPU module, MVME162. Data are passed to an event-builder transmitter in the same VME crate. The overall transfer rate of the subsystem is about 3.5 MB/s.

13.4 Luminosity measurement and the detector performance

The Belle detector started operation in 1999 and an integrated luminosity of about 700 fb^{-1} has been collected by the beginning of 2007.

The *luminosity* of the collider is an important parameter of the experiment. It should be measured continuously during the experiment running for collider-operation monitoring and tuning.

For the Belle detector the on-line luminosity is measured by counting $e^+e^- \to e^+e^-$ events when two final particles constitute a back-to-back

https://doi.org/10.1017/9781009401531.016 Published online by Cambridge University Press

configuration at the endcap parts of the calorimeter with an energy deposition exceeding a high threshold. The rate of these events is about 300 Hz at a luminosity of $\approx 10^{34}\,\mathrm{cm}^{-2}\,\mathrm{s}^{-1}$ which provides a reasonable statistical accuracy at a 10 s integration time.

The total luminosity integrated over a certain period is determined in off-line data analysis using the same process but detected in the barrel calorimeter.

Some examples of the event reconstruction are given in the event displays of Figs. 13.21 and 13.22.

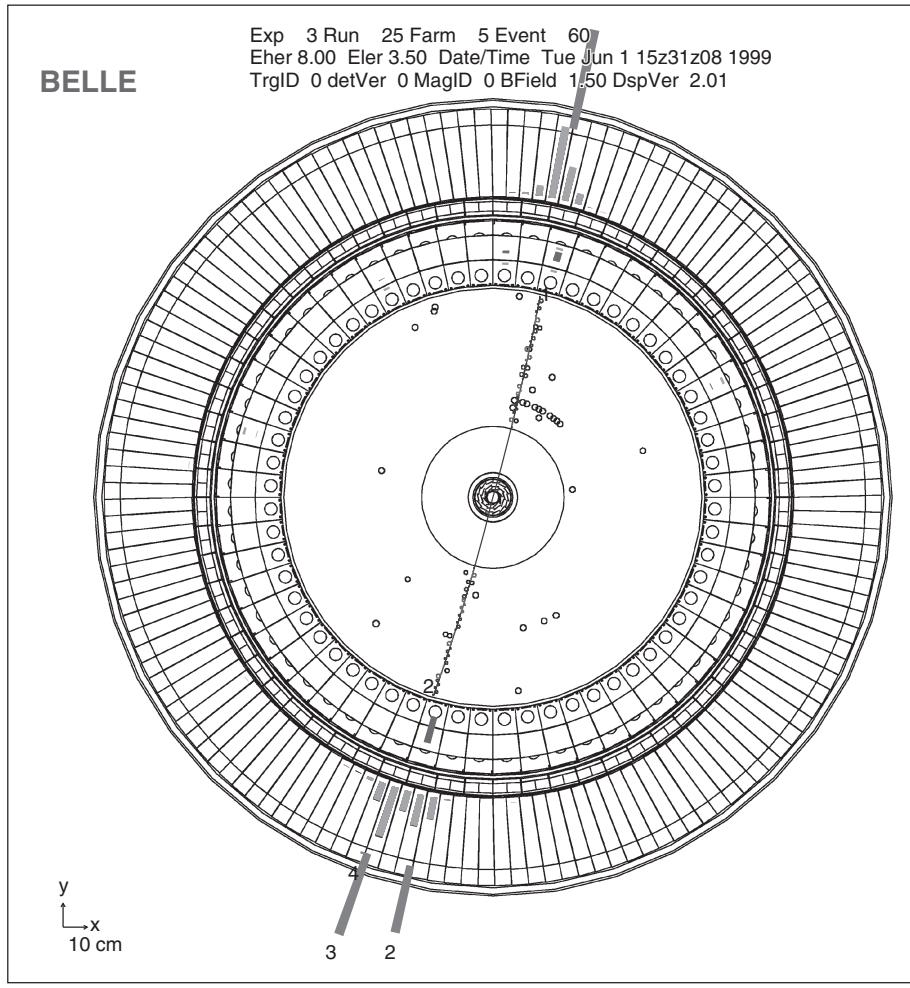

Fig. 13.21. An example of an e^+e^- elastic scattering event ($r\varphi$ projection).

https://doi.org/10.1017/9781009401531.016 Published online by Cambridge University Press

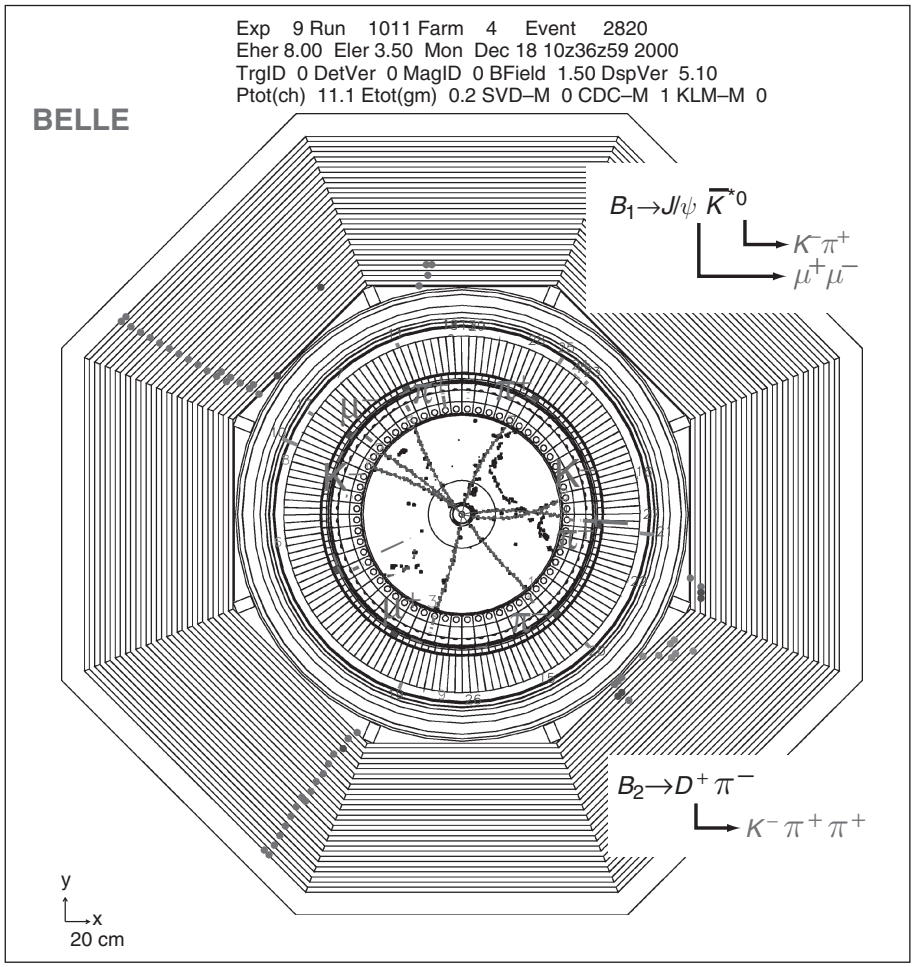

Fig. 13.22. An example of a fully reconstructed $e^+e^- \to B\bar{B}$ event.

The Belle experiment produced a large amount of physics data. The most important results are the observation of CP violation in B-meson decays [20] and the discovery of various new particles [21].

13.5 Problems

13.1 A pion beam passes through a 1.5 m Cherenkov counter that contains CO_2 at 3 atm pressure. At what momentum should the efficiency of the counter reach 50%?

Assume: quantum efficiency of the photomultiplier: 20%, geometrical light collection efficiency: 10%, transfer probability cathode → dynode: 80%.

https://doi.org/10.1017/9781009401531.016 Published online by Cambridge University Press

13.2 In an electron–positron-collider experiment four photons in the final state are recorded ($E_{\gamma_1} = 1\,\text{GeV}$, $E_{\gamma_2} = 1.5\,\text{GeV}$, $E_{\gamma_3} = 1.7\,\text{GeV}$, $E_{\gamma_4} = 0.5\,\text{GeV}$). From the hits in the calorimeter also their relative angles could be determined: $\angle(\gamma_1, \gamma_2) = 6.3°$, $\angle(\gamma_1, \gamma_3) = 12.7°$, $\angle(\gamma_1, \gamma_4) = 160.0°$, $\angle(\gamma_2, \gamma_3) = 23.5°$, $\angle(\gamma_2, \gamma_4) = 85.0°$, $\angle(\gamma_3, \gamma_4) = 34.6°$. Has the photon final state gone through resonances?

13.3 A time-of-flight system allows particles identification in a momentum-defined beam if the energies of relativistic particles are not too high: $\Delta t = \frac{L \cdot c}{2 \cdot p^2} \cdot (m_2^2 - m_1^2)$.

Δt is the time-of-flight difference of the two particles of mass m_1 and m_2 at a flight distance of L. p is the momentum of the particles.

What kind of mass resolution can be achieved if the particles are relativistic and close in mass ($m_1 \approx m_2$)?

Estimate numerical values for the case of $L = 1\,\text{m}$ and a time resolution of $\Delta t = 10\,\text{ps}$ for a mixed muon/pion beam of momentum $1\,\text{GeV}/c$.

13.4 The energies of positron and electron beams colliding in the interaction region of the Belle detector are 3.5 GeV and 8 GeV, respectively. Calculate the total energy in the centre-of-mass system, E_{CM}.

13.5 Estimate the average beam lifetime in the KEKB storage ring in case if the particle losses would be determined by bremsstrahlung on the residual gas in the beam pipe. The KEKB ring circumference is about 3 km and the pressure in the beam pipe is about $10^{-7}\,\text{Pa}$. Assume that the particle leaves the beam when it loses more than 1% of its energy.

13.6 Estimate the rate of the muon-pair production, $e^+e^- \to \mu^+\mu^-$, at the Belle detector for a luminosity of $L = 10^{34}\,\text{cm}^{-2}\,\text{s}^{-1}$ if the muons are detected in a fiducial volume limited by the polar angles ranging from $\theta_0 = 30°$ to $\pi - \theta_0 = 150°$ in the centre-of-mass frame.

References

[1] S. Kurokawa & E. Kikutani, Overview of the KEKB Accelerators, *Nucl. Instr. Meth.* **A499** (2003) 1–7

[2] A. Abashian *et al.* (Belle collaboration), The Belle Detector, *Nucl. Instr. Meth.* **A479** (2002) 117–232

https://doi.org/10.1017/9781009401531.016 Published online by Cambridge University Press

[3] T. Kawasaki, The Belle Silicon Vertex Detector, *Nucl. Instr. Meth.* **A494** (2002) 94–101
[4] R. Abe *et al.*, Belle/SVD2 Status and Performance, *Nucl. Instr. Meth.* **A535** (2004) 379–83
[5] M. Friedl *et al.*, Readout, First- and Second-Level Triggers of the New Belle Silicon Vertex Detector, *Nucl. Instr. Meth.* **A535** (2004) 491–6
[6] H. Hirano *et al.*, A High-Resolution Cylindrical Drift Chamber for the KEK B-factory, *Nucl. Instr. Meth.* **A455** (2000) 294–304
[7] S. Uno *et al.*, Study of a Drift Chamber Filled with a Helium-Ethane Mixture, *Nucl. Instr. Meth.* **A330** (1993) 55–63
[8] O. Nitoh *et al.*, Drift Velocity of Electrons in Helium-based Gas Mixtures Measured with a UV Laser, *Jpn. J. Appl. Phys* **33** (1994) 5929–32
[9] K. Emi *et al.*, Study of a dE/dx Measurement and the Gas-Gain Saturation by a Prototype Drift Chamber for the BELLE-CDC, *Nucl. Instr. Meth.* **A379** (1996) 225–31
[10] Y. Fujita *et al.*, Test of Charge-to-Time Conversion and Multi-hit TDC Technique for the BELLE CDC Readout, *Nucl. Instr. Meth.* **A405** (1998) 105–10
[11] T. Iijima *et al.*, Aerogel Cherenkov Counter for the BELLE Experiment, *Nucl. Instr. Meth.* **A379** (1996) 457–9
[12] T. Sumiyoshi *et al.*, Silica Aerogel Cherenkov Counter for the KEK B-factory Experiment, *Nucl. Instr. Meth.* **A433** (1999) 385–91
[13] T. Iijima *et al.*, Study on fine-mesh PMTs for Detection of Aerogel Cherenkov Light, *Nucl. Instr. Meth.* **A387** (1997) 64–8
[14] H. Yokoyama & M. Yokogawa, Hydrophobic Silica Aerogels, *J. Non-Cryst. Solids* **186** (1995) 23–9
[15] T. Iijima *et al.*, Aerogel Cherenkov Counter for the BELLE Detector, *Nucl. Instr. Meth.* **A453** (2000) 321–5
[16] R. Suda *et al.*, Monte-Carlo Simulation for an Aerogel Cherenkov Counter, *Nucl. Instr. Meth.* **A406** (1998) 213–26
[17] R. Cardarelli *et al.*, Progress in Resistive Plate Counters, *Nucl. Instr. Meth.* **A263** (1988) 20–5
[18] L. Antoniazzi *et al.*, Resistive Plate Counters Readout System, *Nucl. Instr. Meth.* **A307** (1991) 312–15
[19] Y. Ushiroda *et al.*, Development of the Central Trigger System for the BELLE Detector at the KEK B-factory, *Nucl. Instr. Meth.* **A438** (1999) 460–71
[20] K. Abe *et al.* (Belle Collaboration), Observation of Large CP Violation in the Neutral B Meson System, *Phys. Rev. Lett.* **87** (2001) 091802, 1–7; Evidence for CP-Violating Asymmetries in $B^0 \to \pi^+\pi^-$ Decays and Constraints on the CKM Angle φ_2, *Phys. Rev.* **D68** (2003) 012001, 1–15
[21] S.-K. Choi, S.L. Olsen *et al.* (Belle Collaboration), Observation of a New Narrow Charmonium State in Exclusive $B^+ \to K^+\pi^+\pi^- J/\psi$ Decays, *Phys. Rev. Lett.* **91** (2003) 262001, 1–6, hep-ex/0309032 (2003); Observation of the $\eta_c(2S)$ in Exclusive $B \to KK_sK^-\pi^+$ Decays, *Phys. Rev. Lett.* **89** (2002) 102001